

Annealing-inspired training of an optical neural network with ternary weights

Anas Skalli,^{1, a)} Mirko Goldmann,¹ Nasibeh Haghighi,² Stephan Reitzenstein,² James A. Lott,² and Daniel Brunner¹

¹⁾ *FEMTO-ST Institute/Optics Department, CNRS & University Franche-Comté, 15B avenue des Montboucons, Besançon Cedex, 25030, France*

²⁾ *Technical University of Berlin, Hardenbergstraße 36, D-10623 Berlin, Germany*

(Dated: 3 October 2024)

Artificial neural networks (ANNs) represent a fundamentally connectionist and distributed approach to computing, and as such they differ from classical computers that utilize the von Neumann architecture. This has revived research interest in new unconventional hardware to enable more efficient implementations of ANNs rather than emulating them on traditional machines. In order to fully leverage the capabilities of this new generation of ANNs, optimization algorithms that take into account hardware limitations and imperfections are necessary. Photonics represents a particularly promising platform, offering scalability, high speed, energy efficiency, and the capability for parallel information processing. Yet, fully fledged implementations of autonomous optical neural networks (ONNs) with in-situ learning remain scarce. In this work, we propose a ternary weight architecture high-dimensional semiconductor laser-based ONN. We introduce a simple method for achieving ternary weights with Boolean hardware, significantly increasing the ONN's information processing capabilities. Furthermore, we design a novel in-situ optimization algorithm that is compatible with, both, Boolean and ternary weights, and provide a detailed hyperparameter study of said algorithm for two different tasks. Our novel algorithm results in benefits, both in terms of convergence speed and performance. Finally, we experimentally characterize the long-term inference stability of our ONN and find that it is extremely stable with a consistency above 99% over a period of more than 10 hours, addressing one of the main concerns in the field. Our work is of particular relevance in the context of in-situ learning under restricted hardware resources, especially since minimizing the power consumption of auxiliary hardware is crucial to preserving efficiency gains achieved by non-von Neumann ANN implementations.

I. INTRODUCTION

Artificial neural networks (ANNs) represent a fundamentally connectionist and distributed approach to computing, and as such they differ from classical computers that utilize the von Neumann architecture. Over the past decade, ANNs have revolutionized computing¹, disrupting fields ranging from natural language^{2,3} and image processing⁴ to self-driving vehicles⁵ and game playing⁶. The success of these systems is based on their flexibility, high performance in solving abstract tasks, and their fundamentally parallel approach to information processing, allowing them to distill knowledge from large amounts of data. Because they conceptually differ from classical computers, ANNs have to be emulated when running on conventional hardware. This has led, on the one hand, to the meteoric rise of more parallel von Neumann processors such as graphical processing units (GPUs) and application specific tensor processing units (TPUs)⁷. And, on the other hand, it has spurred significant research interest in developing new hardware to enable more efficient implementations of ANNs⁸, often leveraging the strengths of unconventional platforms to either realize co-processors or to build autonomous hardware that directly maps ANN topologies onto the physical substrate.

Although optical neural networks (ONNs) were already demonstrated decades ago^{9,10}, photonics has risen again as a particularly promising platform^{11,12}, offering scalability^{13–15}, high speed^{16–18}, energy efficiency¹⁹, and the capability for parallel information processing^{17,20}. Recent advances in photonic hardware include on-chip integrated tensor cores²¹, and high dimensional optical pre-processors^{22,23}. Among these, semiconductor lasers have emerged as major candidates to implement ONNs due to their ultra-fast modulation rates and complex dynamics¹⁷. Vertical-cavity surface-emitting lasers (VCSELs) are notable for their efficiency, speed, intrinsic nonlinearity, and mature complementary metal-oxide-semiconductor (CMOS) compatible fabrication process^{24,25}.

Reservoir computing (RC)^{26,27} simplifies the use of recurrent neural networks (RNNs) by eliminating the need for intensive back-propagation through time training. In RC, input data is transformed through a high-dimensional network of fixed, interconnected non-linear nodes—the reservoir, and only the output weights are trained. Thus, RC and its closely related extreme learning machine²⁸ can be thought of as the lowest complexity architecture for ANNs, and as such has been implemented on a wide variety of physical substrates²⁹ ranging from electronics³⁰ and spintronics³¹, to optics for ultra-fast information processing using a time-multiplexed approach in^{17,30}, frequency-multiplexed approach in²⁰, and spatial multiplexing in^{32,33}, and mechanical substrates³⁴. Recently, there are also

^{a)} Electronic mail: anas.skalli@femto-st.fr

$f_3 = 6$ mm) adjusting the MMF's image size to approximately the size of the collimated ECL beam on DMD_a. This ensures maximal coupling into the 50 μ m diameter MMF, which through its transmission matrix passively implements the random input weights \mathbf{W}^{rand} for RC.

Following this, the nearfield output of the MMF, $\mathbf{W}^{\text{rand}}\mathbf{u}$, is imaged onto the LA-VCSEL. Here we use a LA-VCSEL with an aperture of ~ 55 μ m and a threshold current of $I_{\text{th}} = 20$ mA. A standard ground-signal-ground (GSG) probe (Microworld MWRF-40A-GSG-200-LP) is used to bias the LA-VCSEL, and the laser is set to $\sim 28^\circ$ C with a thermal stability on the order of 10 mK. The imaging system we use here is also a two lens system. The output of the multimode fibre is collimated using L_4 (THORLABS AC127-20-B-ML, $f_4 = 20$ mm) and imaged onto the large area VCSEL using a microscope objective (MO, OLYMPUS LM-PLN10XIR, $f_{\text{MO}} = 18$ mm). We achieve a magnification factor of $m = f_{\text{MO}}/f_4 = 0.9$, closely matching the MMF's and the LA-VCSEL's apertures. Furthermore, the MMF's numerical aperture (NA) should be chosen such that, considering the effects of magnification m , it is similar but smaller than that of the LA-VCSEL. In our design, the LA-VCSEL's physical properties and dynamics form the reservoir's components, including nonlinear nodes and their interconnections. These nodes, represented by specific areas on the LA-VCSEL's surface, interact through inherent physical mechanisms within the device. Localized Gaussian-like coupling arises from carrier diffusion in the semiconductor quantum wells, while a more complex global coupling is created by the optical field's diffraction within the laser cavity. The LA-VCSEL takes the input information $\mathbf{W}^{\text{rand}}\mathbf{u}$ and transforms it in a complex nonlinear way as is generally the case for optical injection into a semiconductor laser⁴². This process produces the reservoir state \mathbf{x} , and the complexity of the process can be appreciated from the perturbed LA-VCSEL mode profile under injection shown in Fig. 1(b).

Finally, the output layer is realized via DMD_b and a photodetector (DET, Thorlabs PM100A, S150C). By imaging the LA-VCSEL's near field onto DMD_b, we discretize the VCSEL's continuous spatial nonlinear response into a discrete matrix, sampling its surface and thus allowing us to adjust the effective neuron-count for one and the same device through super-pixel size control.

Imaging of the LA-VCSEL onto DMD_b is realized via a two-lens system, using L_5 (THORLABS AC254-100-B-ML, $f_5 = 100$ mm) and MO. The choice of L_5 is motivated by the size of DMD_b's pixels and the characteristic size of features in the LA-VCSEL's mode profile. Ideally, we want to oversample the mode profile with the DMD pixels, which we ensure via magnification $m = f_5/f_{\text{MO}} = 5.55$. The size of speckles on the LA-VCSEL's surface are ~ 5.6 μ m, while the size of one mirror on DMD_b is ~ 13.7 μ m, and taking into account

the magnification every speckle is imaged onto 5 mirrors. The LA-VCSEL is magnified on DMD_b resulting in a diameter of 305 μ m corresponding to an area of 24×24 DMD mirrors. L_6 (THORLABS AC254-150-B-ML, $f_6 = 150$ mm) and L_7 (THORLABS AC254-45-B-ML, $f_7 = 45$ mm) are chosen to demagnify the LA-VCSEL's image to ensure it fits on the DET.

The total area of the rectangular region of interest on DMD_b represents $24 \times 24 = 576$ mirrors in total. Since the LA-VCSEL is circular, its area corresponds to $576 \cdot \pi/4 \simeq 452$ mirrors. We hence achieve approximately 450 fully parallel neurons. The DMD's pixels act as a spatial filter between the LA-VCSEL and the DET, realizing output weights \mathbf{W}^{out} by directing the optical signal associated to DMD_b mirrors to one of the two angular configurations one of which has DET, while signals associated to DMD_b mirrors in the opposite angular configuration are discarded. DMD_b therefore implements a Boolean readout matrix. Through DMD_b, we then tune the spatial positions of the LA-VCSEL that contribute to the optical power detected at DET, and by optimizing this mirror configuration, we train the output \mathbf{y} of the reservoir. Although the DMD is an inherently Boolean, i.e. binary device, we will later in section II B explain how we use it to implement ternary weights.

As shown in Fig. 1(a), a digital computer controls our experiment, sending the input data to be written on DMD_a, recording the output via an oscilloscope as well as controlling the output weights on DMD_b. This computer only acts as a supervisor to our experiment and to implement learning, and as such does not partake in any information processing. It could therefore be replaced by a low-power alternative such as a single board computer like the Raspberry Pi.

The data acquisition loop or forward pass of our ONN is as follows. A batch of N images is loaded on DMD_a's onboard memory to allow for a fast frame rate of 15 kHz. The computer then triggers DMD_a, which in turn hardware triggers the oscilloscope to start the acquisition of the signal detected at DET. Each frame on DMD_a is displayed for 66 μ s, which is orders of magnitude slower than the intrinsic time scales of the LA-VCSEL (~ 1 ns), meaning that we operate the LA-VCSEL in its steady state. The waveform acquired via the oscilloscope is digitally downsampled to N points, yielding the output of the ONN \mathbf{y}^{out} , allowing us to compute an error between this output and a set target $\mathbf{y}^{\text{target}}$, according to the normalized mean square error (NMSE) computed at each epoch k :

$$\text{NMSE}_k = \frac{1}{N \times \text{std}(\mathbf{y}_k^{\text{out}})} \sum_{i=1}^N (\mathbf{y}_k^{\text{out}}(i) - \mathbf{y}^{\text{target}}(i))^2. \quad (1)$$

Following the detailed characterization provided in³²

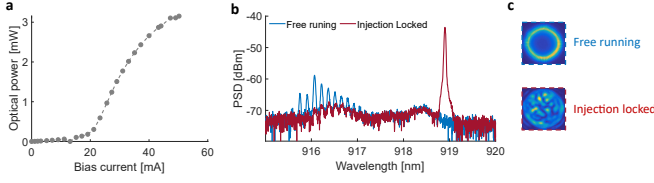


FIG. 2. **Experimental characterization of the LA-VCSEL.** **a** L-I curve of the LA-VCSEL. **b** Spectra of the free running (blue) and injection locked (red) LA-VCSEL. **c** Mode profiles of the free running (blue) and injection locked (red) LA-VCSEL.

and to ensure optimal performance, we operate the LA-VCSEL at $I_{\text{bias}} = 1.5I_{\text{threshold}} \sim 30$ mA, see Fig. 2(a). Moreover, the injection wavelength $\lambda_{\text{inj}} \sim 919$ nm was optimized to yield optimal injection locking conditions as shown in Fig. 2(b), resulting in maximal suppression of the LA-VCSEL's numerous modes when left free, and the injected power is set to match the emission power of the LA-VCSEL yielding an injection power ratio $\text{PR} = P_{\text{inj}}/P_{\text{VCSEL}} \sim 1$. The free-running and injection locked mode profiles of the LA-VCSEL are shown in Fig. 2(c).

B. Ternary weights implementation

A simple, yet powerful change to our previous experimental setup was the implementation of ternary weights, i.e $W^{\text{out}} \in \{-1, 0, +1\}$ with virtually no change to the experiment. Let \mathbf{W}^{out} be our output matrix with ternary entries. We can then define two strictly positive matrices, $\mathbf{W}^{\text{out}+}$ and $\mathbf{W}^{\text{out}-}$ as follows:

$$\mathbf{W}_{ij}^{\text{out}+} = \begin{cases} 1 & \text{if } \mathbf{W}_{ij}^{\text{out}} = 1, \\ 0 & \text{otherwise.} \end{cases}$$

$$\mathbf{W}_{ij}^{\text{out}-} = \begin{cases} 1 & \text{if } \mathbf{W}_{ij}^{\text{out}} = -1, \\ 0 & \text{otherwise.} \end{cases}$$

By sequentially displaying $\mathbf{W}^{\text{out}+}$ and $\mathbf{W}^{\text{out}-}$ and measuring their respective outputs signals, $\mathbf{y}^{\text{out}+}$ and $\mathbf{y}^{\text{out}-}$, the output of our ONN, \mathbf{y}^{out} , is computed by electronic subtraction $\mathbf{y}^{\text{out}} = \mathbf{y}^{\text{out}+} - \mathbf{y}^{\text{out}-}$. Note that, both, $\mathbf{W}^{\text{out}+}$ and $\mathbf{W}^{\text{out}-}$, are positive Boolean matrices that by definition can be displayed on the DMD. The negative weights result from the subtraction of their respective output signals. Figure 3 gives a diagram view of these operations.

However, in its present form, our implementation of ternary output weights results in halving the inference bandwidth due to its sequential nature, requiring two measurements at each step. To remedy this, we could create an optical copy of the LA-VCSEL state on top of DMD_b. Each state would be sent to a separate area of DMD_b, where the corresponding weight matrices $\mathbf{W}^{\text{out}+}$

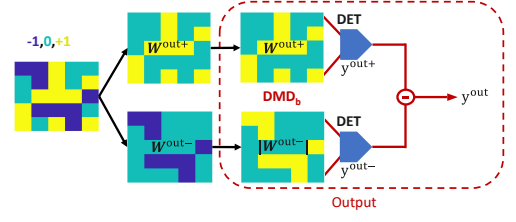


FIG. 3. **Ternary weights implementation.** Diagram showing how we use a single DMD to achieve ternary weights.

and $\mathbf{W}^{\text{out}-}$ would be displayed simultaneously and two outputs would be detected by separate detectors, and their outputs would be subtracted electronically in real-time. This would allow us to maintain the same inference bandwidth as with Boolean weights, while still benefiting from the performance increase provided by ternary weights. A similar concept was already leveraged in the first experimental ONN demonstration⁴³.

C. In-situ learning

Our in-situ optimization algorithm builds upon, and significantly improves the evolutionary algorithm presented in^{44,45} designed for Boolean learning. Originally, a single randomly chosen Boolean weight is inverted at each epoch, and if this change results in a decreased error it is kept, otherwise we revert the Boolean weight to its former value then select a different Boolean weight. Here, instead of simply inverting a single Boolean weight, i.e flipping a mirror, we propose flipping several mirrors per epoch. Furthermore, we make the number of mirrors we flip n^{mirrors} adaptive and proportional to the error according to

$$n^{\text{mirrors}} = \lceil \alpha \cdot \text{NMSE}_k \rceil, \quad (2)$$

where α is a hyperparameter that can be likened to a learning, that does not control step size but rather the number of permutations from one epoch to the next. Setting $\alpha = 0$ corresponds to the original algorithm, the ceiling function $\lceil \cdot \rceil$ ensures that at least one mirror is flipped at each epoch. The pseudo-code for our algorithm and optimization loop is given in algorithm 1.

When using ternary weights, at each epoch instead of simply flipping the state of previously Boolean weights, they are individually assigned a value of either $-1, 0$, or $+1$ with equal probability, making our simple algorithm inherently compatible with Boolean and ternary weights.

This strategy combines elements of random search and a well known gradient free optimization technique known as simulated annealing^{46–48}. Indeed, simulated annealing iteratively optimises a function by applying random fluctuations to the given parameters while only accepting changes that yield positive outcomes in a process similar to a random walk. Crucially, the magnitude of these

random fluctuations depends on a so-called temperature which decreases with time, causing the algorithm to settle at a given position in the landscape. Therefore, our strategy can be viewed as a version of simulated annealing where instead of arbitrarily relying on time to force convergence we directly leverage the error to guide our search in the landscape.

Algorithm 1 Ternary Weights adaptive optimization

```

1: Initialize  $W^{\text{out}}$  randomly
2:  $W^{\text{out\_best}} \leftarrow W^{\text{out}}$ 
3:  $\text{MSE\_best} \leftarrow \text{Forward\_pass}(W^{\text{out}})$ 
4: while not converged do
5:    $n^{\text{mirrors}} \leftarrow \lceil \alpha \times \text{MSE\_best} \rceil$ 
6:    $W^{\text{out\_temp}} \leftarrow W^{\text{out}}$ 
7:   for  $i = 1$  to  $n^{\text{mirrors}}$  do
8:     Randomly select a mirror  $m_i$ 
9:     Randomly set  $W^{\text{out\_temp}}[m_i] \in \{-1, 0, +1\}$ 
10:  end for
11:   $\text{MSE\_temp} \leftarrow \text{Forward\_pass}(W^{\text{out\_temp}})$ 
12:  if  $\text{MSE\_temp} < \text{MSE\_best}$  then
13:     $W^{\text{out}} \leftarrow W^{\text{out\_temp}}$ 
14:     $W^{\text{out\_best}} \leftarrow W^{\text{out\_temp}}$ 
15:     $\text{MSE\_best} \leftarrow \text{MSE\_temp}$ 
16:  else
17:    Revert to  $W^{\text{out}}$ 
18:  end if
19: end while
20: return  $W^{\text{out\_best}}$ 

```

III. RESULTS

A. Benchmark tasks

In order to benchmark our ONN we use two tasks. The first is binary header recognition, the second the is hand-written MNIST dataset. Due to the scalar output given by the single photodetector DET, we use "one-vs-all" classification. For our tests, input sequences \mathbf{u} where comprised of $N = 1000$ images comprised of a 50-50 split between positive and negative examples for one-vs-all classification.

As a reference, for the first task the input data consists of binary pie-shaped headers. The Gaussian input beam is divided into n_{bits} equal sections that encode the header. While seemingly simple, these orthogonal patterns are quite convenient and allow us to reliably scale the dimensionality and complexity of our dataset and computational task. A more detailed description of the encoding used for the binary header can be found in ^{32,33}.

B. Influence of alpha

First let us study the influence of α on convergence. Figure 4 shows the impact of α on the performance and convergence for a 4-bit header recognition task. The error decreases faster for an optimal value of $\alpha = 10$, yet

higher values of α lead to a more unstable learning trajectory. Indeed, flipping more mirrors is akin to bigger steps taken in the search space at each epoch, as such, α behaves much like a learning rate in the context of gradient descent. Moreover, the errors reached by optimal values of α are lower. With $\alpha = 10$ we have $\text{NMSE} = 0.25$ compared to 0.5 for the original algorithm with $\alpha = 0$. This shows that the adaptive strategy is a simple yet powerful modification to the original algorithm. We should note that α is task dependant. Leveraging this improved strategy we are able to increase performance and reach a symbol error rate (SER) of 1.5% for a 6-bit header recognition task.

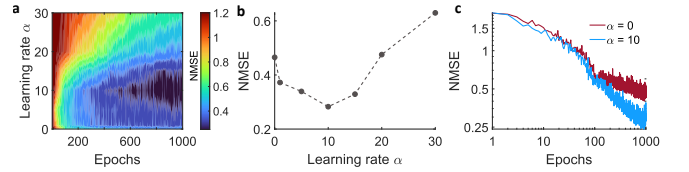


FIG. 4. Impact of hyperparameter α on the learning performance for a 4-bit header recognition task.

Rather than using the synthetic benchmark on binary header recognition, the MNIST task provides a more challenging and genuine image classification problem. Here we study the influence of α on convergence using one-vs-all classification of digits 8 and 9, the hardest in the dataset. Generally speaking, the same trend appears with optimal α values in the range $5 \leq \alpha \leq 20$. Choosing optimal α values results in faster convergence and better performance, allowing the ONN to reach $\sim 85\%$ accuracy for $\alpha = 20$ instead of $\sim 81\%$ for $\alpha = 2$ while converging in ~ 200 epochs as opposed to ~ 600 .

To conclude, our adaptive search strategy offers significant gains both in terms of performance and convergence speed with minimal computational overhead with no changes to the existing hardware, while being compatible with both Boolean and ternary weights.

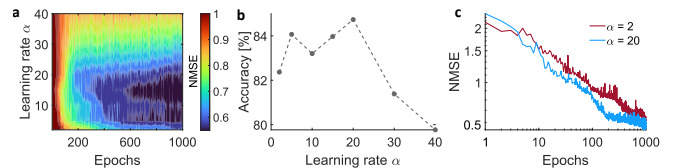


FIG. 5. Impact of tuning hyperparameter α on the learning performance for classification of digit 8 in the MNIST dataset.

C. Benefits of ternary weights

We then experimentally quantify the net gain following the implementation of ternary weights. Figure 6 shows the performance for one-vs-all classification via our ONN for every digit in the MNIST dataset for Boolean and ternary weights. In addition, it also shows the performance for a digital linear classifier trained with ridge regression on the same data. As a reminder we used training and testing sequences \mathbf{u} of length $N = 1000$ images. Crucially, Boolean weights perform poorly, achieving on average $\sim 83.5\%$ classification accuracy on the testing dataset. In contrast, with no physical changes to our experimental setup, we can achieve 90.4% on average with ternary weights approaching the digital linear limit of $\sim 91.8\%$. The performance of our ONN with the LA-VCSEL switched off was also measured with ternary weights as a reference and reaches $\sim 87.2\%$. This corresponds to a more linear hardware system comprised only of the MMF as a passive linear mixing element and the absolute square nonlinearity of optical detection. Yet, as shown in our present measurement, this nonlinearity is not sufficient and cannot result in performance close to a digital linear classifier. Interestingly, our ternary weight ONN with the LA-VCSEL switched off performs better than when the LA-VCSEL is on and using Boolean weights, which means that at this very low-end, weight resolution is a severely limiting factor. Conceptually, because they are positive, Boolean weights cannot exploit nodes or neurons whose responses are anti-correlated with the desired target. The respective weights for these nodes are set to 0 when using Boolean weights which effectively restricts the dimensionality of our ONN.

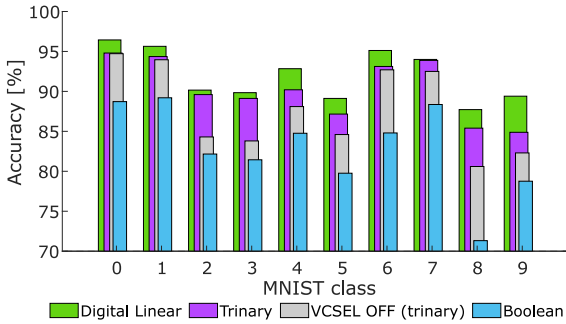


FIG. 6. Performance on the MNIST dataset for Boolean and ternary weights compared to a digital linear classifier.

This comparison highlights how crucial weight resolution and sign can be. Although the performance improvements when using ternary weights are substantial, our ONN still falls short and cannot outperform a digital linear classifier.

D. Long-term stability characterization

The ternary-weight ONN described above performs all processing steps online, reducing the need for additional offline resources. In addition, due to its full hardware implementation, our system is prone to drifts. This makes long-term stability and robustness against drift crucial in our setup. Importantly, these drifts are significantly mitigated through standard proportional-integral-derivative (PID) temperature control of the LA-VCSEL and mechanically securing the injection MMF in place. In our long-term characterization, we find that post learning convergence, the system maintains stable performance for several hours, exhibiting only gradual performance degradation rather than abrupt drops. This stability suggests that continuous, online learning can effectively counteract these slow drifts, maintaining consistent system performance over time.

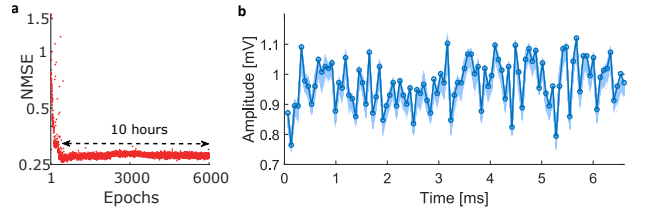


FIG. 7. Long-term stability characterization after learning. **a** NMSE learning curve, after convergence, output weights are fixed and the output is measured every 10 seconds over a period of 10 hours. **b** Output time traces over 10 hours, the first output is shown in bold while following outputs are in a lighter shade. The correlation between responses is $\sim 99.3\%$.

In order to quantify the impact of physical drift on our PNN's performance, we first conducted an optimization loop for 100 epochs, training the ONN to classify digit 0 of MNIST. After convergence to a low error, we kept the output weights fixed and continuously monitored the output of the system every 10 seconds over a period of 10 hours. We were therefore able to measure long-term physical drifts and their impact on computing performance in our system, see Figure 7(a). Surprisingly, the error remains effectively constant over 10 hours with no noticeable drift in terms of performance. Finally, Fig. 7(b) shows the raw output of our setup during these 10 hours, the dark blue line shows the first response at the beginning of the 10 hours, and the light blue shows the next responses over the duration of the experiment. Importantly, the correlation between responses, i.e. consistency⁴⁹, after learning is $\sim 99.3\%$, showcasing how even with our simple control schemes we can greatly minimize instabilities in our system.

It should be noted that, because the inference speed is orders of magnitude slower than the dynamics of the VCSEL, we do not measure the dynamical stability of our device on the timescale of its inherent dynamics. We

rather measure a time averaged or steady state response output of the LA-VCSEL, which together with injection locking further increases stability.

IV. CONCLUSION

We significantly improved upon our previous LA-VCSEL based ONN, by demonstrating an efficient and low complexity method to implement ternary weights that is broadly compatible with Boolean-weight based RC. Crucially, we report significant improvements in performance with no physical changes to our experimental setup.

In addition, we introduced a novel in-situ optimization algorithm that is compatible with, both, Boolean and ternary weights. We provided a detailed hyperparameter study of said algorithm for two different tasks, and experimentally verified its benefits in terms of convergence speed and performance gain, resulting in an increase of 7% on average when going from Boolean to ternary weights. We also confirmed that weight resolution is the main limiting factor in our relatively low neuron-count ONN, offering a clear avenue for future improvements. Finally, we experimentally characterized the long-term inference stability of our ONN and found that it was extremely stable with a consistency above 99% over a period of more than 10 hours. Our work is of high relevance in the context of in-situ learning particularly under restricted hardware resources.

DECLARATIONS

The authors acknowledge the support of the Region Bourgogne Franche-Comté. This work was supported by the EUR EIPHI program (Contract No. ANR-17-EURE-0002), by the Volkswagen Foundation (Neuro-QNet I&II), by the French Investissements d’Avenir program, project ISITE-BFC (contract ANR-15-IDEX-03), and by the German Research Foundation (via SFB 787), and by the European Union’s Horizon research and innovation program under the Marie Skłodowska-Curie grant agreement No 860830 (POST DIGITAL) and 101044777 (INSPIRE).

AUTHOR CONTRIBUTION

AS and DB conceived the experiment and in combination with MG developed the learning algorithm. NH fabricated and characterized the LA-VCSEL and many neighboring devices under the supervision of JL to select a suitable VCSEL for the experiment using VCSEL wafers designed and provided by JL. SR provided the fabrication infrastructures. AS carried out all experiments under the supervision of DB, AS wrote the manuscript with contributions of all authors.

Components	Reference
ECL	TOPTICA CTL 950
SMF	
L_1	THORLABS C110TMD-B)
DMD_a	Vialux XGA 0.7" V4100
L_2	THORLABS C110TMD-B
L_3	THORLABS AC508-150-B-ML
MMF	THORLABS M42L01
L_4	THORLABS AC127-20-B-ML
BS 90 : 10	THORLABS BSX11R
BS 50 : 50	THORLABS CCM1-BS014/M
MO	OLYMPUS LMPLN10XIR
VCSEL	Custom made in university cleanroom
L_5	THORLABS AC254-100-B-ML
DMD_b	Vialux XGA 0.7" V4100
L_6	THORLABS AC254-150-B-ML
L_7	THORLABS AC254-45-B-ML
DET	THORLABS PM100A, S150C
Oscilloscope	ROHDE SCHWARZ RTO 1084
PC	Standard Dell Precision i5-6400 8Gb RAM
BS 10 : 90	THORLABS BSN11R
L_{OSA}	THORLABS AC254-35-B-ML
MMF	THORLABS M42L01
OSA	Yokogawa AQ6370D
L_{CAM}	THORLABS AC254-100-B-ML
CAM	IDS-UI-LI348x-E

TABLE I. Table showing all components in the optical setup for reference.

V. LIST OF OPTICAL COMPONENTS

VI. BIBLIOGRAPHY

- ¹Y. LeCun, Y. Bengio, and G. Hinton, *nature* **521**, 436 (2015).
- ²J. Achiam, S. Adler, S. Agarwal, L. Ahmad, I. Akkaya, F. L. Aleman, D. Almeida, J. Altenschmidt, S. Altman, S. Anadkat, *et al.*, arXiv preprint arXiv:2303.08774 (2023).
- ³A. Vaswani, N. Shazeer, N. Parmar, J. Uszkoreit, L. Jones, A. N. Gomez, L. Kaiser, and I. Polosukhin, *Advances in neural information processing systems* **30** (2017).
- ⁴V. ARD and J. GR, *Nature* **609** (2022).
- ⁵C. Badue, R. Guidolini, R. V. Carneiro, P. Azevedo, V. B. Cardoso, A. Forechi, L. Jesus, R. Berriel, T. M. Paixao, F. Mutz, *et al.*, *Expert systems with applications* **165**, 113816 (2021).
- ⁶D. Silver, T. Hubert, J. Schrittwieser, I. Antonoglou, M. Lai, A. Guez, M. Lanctot, L. Sifre, D. Kumaran, T. Graepel, *et al.*, *Science* **362**, 1140 (2018).
- ⁷A. Reuther, P. Michaleas, M. Jones, V. Gadepally, S. Samsi, and J. Kepner, in *2020 IEEE high performance extreme computing conference (HPEC)* (IEEE, 2020) pp. 1–12.
- ⁸S. Hooker, *Communications of the ACM* **64**, 58 (2021).
- ⁹D. Psaltis, D. Brady, and K. Wagner, *Applied Optics* **27**, 1752 (1988).
- ¹⁰D. Psaltis, A. Sideris, and A. A. Yamamura, *IEEE control systems magazine* **8**, 17 (1988).
- ¹¹P. L. McMahon, *Nature Reviews Physics* **5**, 717 (2023).
- ¹²S. Abreu, I. Boikov, M. Goldmann, T. Jonuzi, A. Lupo, S. Masaad, L. Nguyen, E. Picco, G. Pourcel, A. Skalli, *et al.*, *Reviews in Physics*, 100093 (2024).
- ¹³N. U. Dinc, D. Psaltis, and D. Brunner, *Photoniques*, 34 (2020).
- ¹⁴M. Rafayelyan, J. Dong, Y. Tan, F. Krzakala, and S. Gigan, *Physical Review X* **10**, 041037 (2020).

- ¹⁵J. Moughames, X. Porte, M. Thiel, G. Ulliac, L. Larger, M. Jacquot, M. Kadic, and D. Brunner, *Optica* **7**, 640 (2020).
- ¹⁶Y. Shen, N. C. Harris, S. Skirlo, M. Prabhu, T. Baehr-Jones, M. Hochberg, X. Sun, S. Zhao, H. Larochelle, D. Englund, *et al.*, *Nature Photonics* **11**, 441 (2017).
- ¹⁷D. Brunner, M. C. Soriano, C. R. Mirasso, and I. Fischer, *Nature communications* **4**, 1 (2013).
- ¹⁸Z. Chen, A. Sludds, R. Davis III, I. Christen, L. Bernstein, L. Ateshian, T. Heuser, N. Heermeier, J. A. Lott, S. Reitzenstein, *et al.*, *Nature Photonics* **17**, 723 (2023).
- ¹⁹D. A. Miller, *Journal of Lightwave Technology* **35**, 346 (2017).
- ²⁰A. Lupo, E. Picco, M. Zajnulina, and S. Massar, *Optica* **10**, 1478 (2023).
- ²¹J. Feldmann, N. Youngblood, M. Karpov, H. Gehring, X. Li, M. Stappers, M. Le Gallo, X. Fu, A. Lukashchuk, A. S. Raja, *et al.*, *Nature* **589**, 52 (2021).
- ²²T. Wang, M. M. Sohoni, L. G. Wright, M. M. Stein, S.-Y. Ma, T. Onodera, M. G. Anderson, and P. L. McMahon, *Nature Photonics* **17**, 408 (2023).
- ²³F. Xia, K. Kim, Y. Eliezer, L. Shaughnessy, S. Gigan, and H. Cao, *arXiv preprint arXiv:2307.08558* (2023).
- ²⁴M. Muller, W. Hofmann, T. Grundl, M. Horn, P. Wolf, R. D. Nagel, E. Ronneberg, G. Bohm, D. Bimberg, and M.-C. Amann, *IEEE Journal of selected topics in Quantum Electronics* **17**, 1158 (2011).
- ²⁵J. Vatin, D. Rontani, and M. Sciamanna, *Optics letters* **43**, 4497 (2018).
- ²⁶H. Jaeger, Bonn, Germany: German National Research Center for Information Technology GMD Technical Report **148**, 13 (2001).
- ²⁷W. Maass, T. Natschlager, and H. Markram, *Neural computation* **14**, 2531 (2002).
- ²⁸S. Ortín, M. C. Soriano, L. Pesquera, D. Brunner, D. San-Martín, I. Fischer, C. Mirasso, and J. Gutiérrez, *Scientific reports* **5**, 14945 (2015).
- ²⁹G. Tanaka, T. Yamane, J. B. Héroux, R. Nakane, N. Kanazawa, S. Takeda, H. Numata, D. Nakano, and A. Hirose, *Neural Networks* **115**, 100 (2019).
- ³⁰L. Appeltant, M. C. Soriano, G. Van der Sande, J. Danckaert, S. Massar, J. Dambre, B. Schrauwen, C. R. Mirasso, and I. Fischer, *Nature communications* **2**, 1 (2011).
- ³¹D. Marković, N. Leroux, M. Riou, F. Abreu Araujo, J. Torreon, D. Querlioz, A. Fukushima, S. Yuasa, J. Trastoy, P. Bortolotti, *et al.*, *Applied Physics Letters* **114** (2019).
- ³²A. Skalli, X. Porte, N. Haghighi, S. Reitzenstein, J. A. Lott, and D. Brunner, *Optical Materials Express* **12**, 2793 (2022).
- ³³X. Porte, A. Skalli, N. Haghighi, S. Reitzenstein, J. A. Lott, and D. Brunner, *Journal of Physics: Photonics* **3**, 024017 (2021).
- ³⁴K. Nakajima, H. Hauser, R. Kang, E. Guglielmino, D. G. Caldwell, and R. Pfeifer, *Front. Comput. Neurosci.* **7**, 91 (2013).
- ³⁵D. Marković and J. Grollier, *Applied physics letters* **117** (2020).
- ³⁶L. G. Wright, T. Onodera, M. M. Stein, T. Wang, D. T. Schachter, Z. Hu, and P. L. McMahon, *Nature* **601**, 549 (2022).
- ³⁷A. Momeni, B. Rahmani, B. Scellier, L. G. Wright, P. L. McMahon, C. C. Wanjura, Y. Li, A. Skalli, N. G. Berloff, T. Onodera, *et al.*, *arXiv preprint arXiv:2406.03372* (2024).
- ³⁸D. Brunner and D. Psaltis, *Nature Photonics* **15**, 323 (2021).
- ³⁹R.-J. Zhu, Y. Zhang, E. Sifferman, T. Sheaves, Y. Wang, D. Richmond, P. Zhou, and J. K. Eshraghian, *arXiv preprint arXiv:2406.02528* (2024).
- ⁴⁰T. Hirtzlin, M. Bocquet, B. Penkovsky, J.-O. Klein, E. Nowak, E. Vianello, J.-M. Portal, and D. Querlioz, *Frontiers in neuroscience* **13**, 1383 (2020).
- ⁴¹A. Laborieux, M. Bocquet, T. Hirtzlin, J.-O. Klein, L. H. Diez, E. Nowak, E. Vianello, J.-M. Portal, and D. Querlioz, in *2020 2nd IEEE International Conference on Artificial Intelligence Circuits and Systems (AICAS)* (IEEE, 2020) pp. 136–140.
- ⁴²K. Hicke, M. A. Escalona-Morán, D. Brunner, M. C. Soriano, I. Fischer, and C. R. Mirasso, *IEEE Journal of Selected Topics in Quantum Electronics* **19**, 1501610 (2013).
- ⁴³N. H. Farhat, D. Psaltis, A. Prata, and E. Paek, *Applied optics* **24**, 1469 (1985).
- ⁴⁴J. Bueno, S. Maktoobi, L. Froehly, I. Fischer, M. Jacquot, L. Larger, and D. Brunner, *Optica* **5**, 756 (2018).
- ⁴⁵L. Andreoli, X. Porte, S. Chrétien, M. Jacquot, L. Larger, and D. Brunner, *Nanophotonics* **9**, 4139 (2020).
- ⁴⁶P. J. Van Laarhoven, E. H. Aarts, P. J. van Laarhoven, and E. H. Aarts, *Simulated annealing* (Springer, 1987).
- ⁴⁷S. Kirkpatrick, C. D. Gelatt Jr, and M. P. Vecchi, *science* **220**, 671 (1983).
- ⁴⁸D. Bertsimas and J. Tsitsiklis, *Statistical science* **8**, 10 (1993).
- ⁴⁹K. Kanno and A. Uchida, *Physical Review E* **86**, 066202 (2012).